Astronomy
&
Astrophysics

Evidence of a type 1/type 2 dichotomy in the correlation between quasar optical polarization and host-galaxy/extended emission position angles[⋆,⋆⋆]

B. Borguet[⋆⋆⋆], D. Hutsemékers[†], G. Letawe, Y. Letawe, and P. Magain

Institut d'Astrophysique et de Géophysique, University of Liège, Allée du 6 Août 17, 4000 Liège, Belgium
e-mail: b.borguet@ulg.ac.be

ABSTRACT

Aims. For Seyfert galaxies, the AGN unification model provides a simple and well-established explanation of the type 1/type 2 dichotomy through orientation-based effects. The generalization of this unification model to the higher luminosity AGNs that quasars are remains a key question. The recent detection of type 2 radio-quiet quasars seems to support such an extension. We propose a further test of this scenario.
Methods. On the basis of a compilation of quasar host-galaxy position angles consisting of previously published data and of new measurements performed using HST Archive images, we investigate the possible existence of a correlation between the linear polarization position angle and the host-galaxy/extended emission position angle of quasars.
Results. We find that the orientation of the rest-frame UV/blue extended emission is correlated to the direction of the quasar polarization. For type 1 quasars, the polarization is aligned with the extended UV/blue emission, while these two quantities are perpendicular in type 2 objects. This result is independent of the quasar radio loudness. We interpret this (anti-)alignment effect in terms of scattering in a two-component polar+equatorial model that applies to both type 1 and type 2 objects. Moreover, the orientation of the polarization –and then of the UV/blue scattered light– does not appear correlated to the major axis of the stellar component of the host-galaxy measured from near-IR images.

Key words. galaxies: quasars: general – polarization

1. Introduction

The study of quasars shows that we can classify them in various categories. Radio-loud quasars (RLQ) are distinguished from the radio-quiet quasars (RQQ) according to their radio power (Kellerman et al. 1989), and the type 1/type 2 objects by the presence or absence of broad emission lines in their spectrum (Lawrence 1987).

One can then wonder whether a common link exists between all these objects; i.e. are the physical processes at the origin of all quasars the same? An interesting way to tackle this question consists in the use of the linear optical polarization. Polarimetry, in combination with spectroscopy, has led to major advances in the development of a unified scheme for AGN (see Antonucci 1993 for a review). The discovery of hidden broad emission lines in the polarized spectrum of the type 2 Seyfert galaxy NGC 1068 led to considering these objects as intrinsically identical to type 1 Seyfert, the edge-on orientation of a dusty torus blocking both the direct view of the central engine and the broad emission line region (Antonucci & Miller 1985).

The question we investigate in this paper relates to the possible existence of a correlation between the optical polarization position angle θ_{Pola}[1] and the orientation of the host-galaxy/extended emission PA_{host}[2] in the case of RLQs and RQQs. The relation between quasars and their host galaxies may play a fundamental role in our understanding of the AGN phenomenon and in determining the importance of the feedback of AGN on their hosts.

Such a correlation has already been studied in the case of the Seyfert galaxies (less powerful AGNs). Thompson & Martin (1988) found a tendency for Seyfert 1 to have their polarization angle aligned with the major axis of their host-galaxy, an observation that they interpreted as the dichroic extinction by aligned dust grains in the Seyfert host-galaxy. In the case of the quasars, Berriman et al. (1990) investigated this question. They determined the PA_{host} of 24 PG quasars by hand from ground-based images and computed the acute angle $\Delta\theta$ between θ_{Pola} and PA_{host}. They observed that, while more objects seem to appear at low values ($\Delta\theta \leq 45°$), this effect was only marginally statistically significant.

Investigating this problem with ground-based data for type 1 quasars is hampered by the inability of separating the faint

---

[1] The polarization position angle θ_{Pola} is defined as the position angle of the maximal elongation of the electric vector in the plane of polarization, measured in degrees east of north.

[2] The orientation of the host-galaxy PA_{host} is characterized by the position angle of its major axis projected onto the plane of the sky, measured in degrees east of north.

host-galaxy/extended emission[3] from the blinding light of the quasar nucleus. Because of its high angular resolution and stable point spread function (PSF), the Hubble Space Telescope (HST) permits a proper removal of the contribution of the powerful quasar nucleus, thus allowing the investigation of the host-galaxy parameters. A large number of quasar-host observing programs were carried out with the HST leading to a statistically useful sample of quasar host-galaxy parameters (e.g. Bahcall et al. 1997; Dunlop et al. 2003 and many more; see Sects. 2 and 3). Our aim is to investigate the θ_{Pola}/PA$_{host}$ relation on the basis of high-resolution HST quasar images. We use either position angles given in the literature or the PA$_{host}$ we measured ourselves from HST Archive observations (hereafter called "*new* PA$_{host}$ *data*").

The layout of this paper is as follows. In Sect. 2 we introduce the samples of quasars used in this study that possess a PA$_{host}$ given in the literature. In Sect. 3, we outline the samples with good imaging data but for which no PA$_{host}$ were published, and we summarize our data analysis process and the approach followed to model the HST Archive images and to derive the host-galaxy parameters. In Sect. 4 we briefly describe the polarization and radio data. Then in Sect. 5 we present the statistical analysis of the sample and the results obtained. In Sect. 6 we discuss the results and compare them to former studies. Finally, our conclusions are summarized in Sect. 7.

2. Description of the sample: published data

In this section we give details about the observing campaigns used in the present study except for the *new* PA$_{host}$ *data*, which will be discussed in the next section. Note that our study is essentially based on intrinsically high luminosity radio-loud and radio-quiet AGN (i.e. quasars), but does not consider BLLac objects, since these objects show highly variable luminosity and polarization (e.g. Urry & Padovani 1995). We also select the type 2 counterpart of radio-loud quasars (the narrow-line radio galaxies, NLRGs, Barthel 1989) from the whole RG sample on the basis of the classifications given in the literature (Grandi et al. 2006; Haas et al. 2005; Cohen et al. 1999; Rudy et al. 1983; Tadhunter et al. 1998; Tadhunter et al. 2002; van Bemmel & Bertoldi 2001; Siebenmorgen et al. 2004; Jackson & Rawlings 1997).

In the following we present the samples that were analyzed in the literature and the methods used by authors to recover the host-galaxy parameters from the quasar images. For more suitability in the following text, we use the convention as *Ba97* of refering to the images/data published in the paper of Bahcall et al. (1997), and so on for the other papers.

Note that, in our final sample, we only consider objects from these samples if they actually possess both a reliable host position angle and an accurate enough polarization angle, so only part of the objects presented in the papers belong to our final sample. A detailed description of the observations and PA$_{host}$ measurements is available in Appendix A.1.

The visible domain: this sample is constituted of data published in the following papers, chronologically ordered: Cimatti et al. (1993), Disney et al. (1995), de Koff et al. (1996), Lehnert et al. (1999), Martel et al. (1999), Dunlop et al. (2003),

Floyd et al. (2004), and McLure et al. (2004), respectively abbreviated *Ci93*, *Di95*, *Dk96*, *Le99*, *Ma99*, *Du03*, *Fl04*, and *Mc04*.

The radio galaxy and quasar images studied in these papers were mostly (except the RGs from *Ci93*) imaged through an *R*-band filter with the HST WFPC2 camera. The sample spans a redshift range of $z = 0.0$ to $z = 2.0$ and is essentially made out of 3CR and PG objects. Considering these samples, we obtain a final number of 79 objects possessing a published PA$_{host}$ in the visible domain, together with a polarization position angle.

The near-IR domain: the near-IR compilation contains several samples coming from surveys using the NICMOS HST camera or ground based images. All the targets of the resulting sample were observed in the near-IR using *K* and *H*-band filters. The host-galaxy data were retrieved from the papers of Taylor et al. (1996), Percival et al. (2001), Guyon et al. (2006), and Veilleux et al. (2006) abbreviated respectively *Ta96*, *Pe01*, *Gu06* and *Ve06*. The compiled resulting sample, considering only the objects for which we have at least a PA$_{host}$ and a polarization position angle contains 21 objects with redshifts $z \leq 0.4$.

Determination of the PA$_{host}$: the PA$_{host}$ published in the aforementioned papers were measured as follows. The first step determining the position angle of a quasar host-galaxy is the proper subtraction of the bright central source that dominates the optical emission of type 1 objects. To this aim, a careful PSF construction is realized in order to precisely characterize the profile of a point-like source imaged by a given instrument. This PSF is then scaled to the quasar intensity and subtracted from the quasar image, allowing in most cases the detection of the underlying host. This first step is realized for all quasars except for type 2 objects in which the heavy obscuration of the central source provides a non-contaminated view of the host.

Several techniques are then used to derive the host parameters (PA$_{host}$ and b/a) either ellipse-fitting on the host image, followed by measuring the model position angle at a chosen surface brightness, or two-dimensional galaxy profile fitting over the nucleus-subtracted image. These techniques give fairly similar results since the crucial step remains the proper separation between the point-like component and the underlying host.

3. Measurements of new PA$_{host}$

The samples are made up of available quasar/RG HST observations retrieved from the Archive, for which the images and, more particularly, the host-galaxy parameters were not thoroughly studied or published in the literature. Detailed observational properties of these samples are available in Appendix A.2, while major properties are summarized in Table 1.

The visible domain: this sample gathers quasars imaged in the *V* to *R*-band using the HST WFPC2 or ACS camera. The total sample consists of 53 objects coming from the following papers: Bahcall et al. (1997), Boyce et al. (1998), Marble et al. (2003), and Zakamska et al. (2006), hereafter abbreviated *Ba97*, *Bo98*, *Ma03*, and *Za06*, respectively. This sample essentially contains $z \leq 0.5$ 3CR, 2-Micron All Sky Survey (2MASS), Sloan Digital Sky Survey (SDSS), and PG quasars.

The near-IR domain: this sample is a compilation of 17 RQQs and RLQs from the McLeod et al. (2001) and

---

[3] In the following, we use indifferently the term host galaxy or extended emission to refer to all the extended emission around the central source including stars, ionized gas or scattered light.

Table 1. Characteristics of the surveys used to derive new host-galaxy position angles.

Reference[a]	Prop ID[b]	Instrument[c]	Filter[d]
Ba97	5343, 5099	WFPC2-WF3	F606M
Bo98	6303, 5143	WFPC2-PC1	F702M
Ml01	7421	NICMOS-NIC2	F160M
Ku01	7447	NICMOS-NIC1	F110M&F165M
Ma03	9057	WFPC2-PC1	F814M
Za06	9905	ACS-WFC	F550M

[a] Reference to the paper where the images were published.
[b] Corresponding HST Proposal ID. [c] Name of the camera. [c] Name of the filter used.

Kukula et al. (2001) papers (hereafter abbreviated *Ml01* and *Ku01*). The objects, spanning a redshift range $0.1 < z < 2.0$ were observed through the *H* or *J*-band by the NICMOS camera on board HST.

3.1. The method

Here we describe the method we used to derive host-galaxy position angle and axial ratio from the images. First we outline the images reduction steps and then we give an overview of the technique used to disentangle the quasar nuclear and host-galaxy contributions. We then present the construction of the PSF necessary for an accurate separation. The results of the modeling are finally given and compared to the results of other studies in the following section.

3.1.1. Image reduction

The quasar images were retrieved from the MAST HST Archive of the Space Telescope Science Institute (STScI, http://archive.stsci.edu/astro). All the images had already been pre-processed by standard STSDAS pipeline software adapted to each HST instrument. This pre-processing essentially consists in dark-frame and bias substraction along with flat-fielding, with the best reference files available. In the case of the ACS images, where the geometric distortion in the WFC camera is significant, an additional step was added to correct these distortions thanks to the *MultiDrizzle* routine (Koekemoer et al. 2002).

In addition to this pre-processing, we carried out two additional processing steps. The first consists in removing cosmic rays using the *crrej* task of the Image Reduction and Analysis Facility (IRAF) software that rejects high pixels from sets of exposures of the same field in an iterative way. These bad pixels are not used in the creation of the output image, thereby providing a final cosmic-ray free image. In the case of the NICMOS data, this step is not essential since the MULTIACCUM mode used in the image acquisition phase already realizes this processing when acquiring the data (Schultz et al. 2005).

The second step consists in background subtraction. As the backgrounds on the WFPC2 and ACS WFC camera are extremely flat around the targets of interest, we simply estimated the mean of the background level in each image from several subsets of pixels excluding obvious sources, and then subtracted this mean value to each pixel of the image. In the case of the NICMOS data, the known pedestal effect (variable quadrant bias of the detectors) was not taken into account, since the objects images were always almost centered in one of the quadrants.

3.1.2. Image processing

As our primarily aim is to determine the position angle of the host-galaxy surrounding nuclear-dominated objects, we have to distinguish the faint fuzz of the galaxy from the quasar. The use of high-resolution HST images partly solves this problem, but raises another one: the complex path of the light rays in the instrument creates a complex PSF with quite extended wings that can cover the underlying galaxy. The use of a deconvolution technique makes it possible to separate the light of the point-like quasar central source (roughly a scaled PSF) quite efficiently from the light of the host. We used a version of the MCS algorithm (Magain et al. 1998) that is well-suited to deconvolving the HST images while adjusting an analytical galaxy model.

Our image processing proceeds in essentially two steps. In the first stage, the parameters (intensity and position) of the point source are adjusted to subtract the contribution of the quasar. This contribution is estimated so that a minimal amount of PSF structure remains in the image. This step has to be realized with particular care as the inner pixels (out to a radius of 5 pixels for the extreme cases) of the quasar image may be saturated, so that the PSF subtraction process may become quite subjective.

The second stage corresponds to the fitting of an analytical galaxy profile (properly convolved with the HST PSF) to the PSF-subtracted images. The analytic profile we used consists in a typical Sérsic (Sérsic 1968) profile:

$$I(x, y) = I_0 \, e^{-(Ax^2 + By^2 + Cxy)^\alpha} \qquad (1)$$

where I_0 stands for the central surface brightness, and α describes its profile (the profile is called elliptical or *de Vaucouleurs* if $\alpha = 1/8$ and spiral or disk-like if $\alpha = 1/2$). A coordinate change allows us to recover the axial ratio (b/a) and the position angle (PA_{host}) of the model fitted to the data. Since we are essentially interested in the orientation of the major light concentration, we only use a *de Vaucouleurs* profile in the following, noting after some tests that PA_{host} does not strongly depend on α.

3.1.3. PSF creation

The quality of the image processing critically depends on the accuracy of the PSF used. A careful construction of the PSF is of prime importance to properly separate the contribution of the bright nucleus from that of the host-galaxy. In the MCS method adapted to HST images, the construction of the PSF proceeds in two steps. The first step consists in fitting a sub-sampled numerical estimate of the PSF computed with the TinyTim package (Krist & Hook 2004) to an original resolution one (also estimated with TinyTim). This step provides the *Tinydec* i.e. a PSF that has a better resolution than the observed one. The second step consists in a second fit, where the *Tinydec* is fitted to an observed PSF (typically a calibration star lying in a weakly crowded field) in order to improve the agreement between the numerical estimate and the observed point source. This second fit is important since the TinyTim package is unable to give an accurate estimation of the external, fainter halo ($r > 2''$), as well as of the diffraction spikes (McLure et al. 2000; Pian et al. 2002).

Usually one or more stars were imaged during each of these campaigns with growing exposures times, allowing the construction of a deep, unsaturated PSF star. The aforementioned procedure could not be used in the case of the *Ma03* and *Za06* campaigns, since no time was devoted to the observation of a specific PSF star, then forcing us to use the *Tinydec* as the PSF. However, the lack of observed standard PSF star is less constraining in

these two cases since the imaged quasars are generally heavily obscured objects, such that the central source contribution and the intensity of the associated scattered halo are weak (or null for the type 2 objects of *Za06*).

3.1.4. The error frame

To determine whether a given quasar model accurately describes of an observed image, a χ^2 minimization is used by the MCS program:

$$\chi^2 = \sum_{\text{allpixels}} \left[\frac{Image - (PointSource + Host) \otimes PSF}{\sigma} \right]^2, \qquad (2)$$

where *Image* represents the reduced quasar image, *PointSource + Host* the quasar model, and σ the standard deviation in the corresponding pixel (called the error frame). A careful construction of the error frame is mandatory for each image to avoid biased results.

The error term accounts for different elements: first, for a Poissonian component due to photon shot noise and dark current, as well as the noise induced by the CCD readout. The second component accounts for the detector pixels that are known to work badly, these pixels being indexed in flag frames available via the STScI website. We used this frame to construct masks such that zero weight (i.e. $1/\sigma = 0$) is allocated to these indexed pixels, while this value is set to one everywhere else over the frame. The last component accounts for saturated regions in the observed image due to the long exposure time required for imaging faint host galaxies. We accounted for this final component by assigning a null weight to the implied pixels. These masks are then multiplied by the original $1/\sigma$ constructed in the first step.

3.2. The resulting PA_host

The results of our image analysis are summarized in Table 2. Columns are as follows: (1) object name, (2) redshift of the object, (3) radio-loudness of the object (RL or RQ), (4) source of the image, (5) spectral domain of the image (visible (Vis) or near-IR (NIR)), (6) type of the host galaxy (E: elliptical, S: spiral and U: undefined); (7) and (8) axial ratio and position angle of the host (PA_host in degrees, east of north) and (9) a quality criterion (1, 2, or 3, with 1 being the highest quality). The parameters in Cols. (6) and (9) are defined in the following subsections.

Figure 1 illustrates the results for two representative objects of our *new* PA_host *data* sample. From left to right, we show for each object the final reduced HST image, a closer view on the PSF-subtracted image, the host-galaxy model fitted over the PSF-subtracted image and the model-subtracted residual image (darker regions account for un-modeled details such as spiral arms, interaction features, etc.).

3.2.1. Morphology of the host

As we use only a *de Vaucouleurs* model to derive the host-galaxy parameters, we cannot provide a host morphology classification on the basis of a better description of the host by a spheroidal or a disc-like profile. The morphological classification was thus realized by careful visual inspection of both the PSF-subtracted image and the model-subtracted residual image. We adopted a classification scheme similar to the one defined in Guyon et al. (2006): if a bar or spiral arms was obvious in one image, the host was classified as a spiral (disk-present) and abbreviated by S in

Table 2. If no spiral structure or bar was visible in the image, we classified the host as an elliptical galaxy (E). The remaining host galaxies (those presenting strong interaction traces/complex morphology, multiple nuclei, etc.) were assigned to the "undefined" class (abbreviated U). Finally, in some cases no host-galaxy was detected even after PSF-subtraction, essentially due to the comparatively high redshift or to the insensitivity to low surface brightness features because of short exposure times.

3.2.2. Reliability and error estimates

The b/a and PA_host reported in Table 2 were determined within uncertainties that essentially come from the degeneracy existing between the host-galaxy model and the estimated nuclear contribution. These uncertainties were quite difficult to estimate, especially in our case where the objects come from samples with different observational circumstances.

A useful test when estimating the uncertainties of the derived parameters is proposed in *Fl04*: to ensure that the modeling routines of the host reach the global minimum within the six-dimensional model parameter space, they used six different starting points for each object close to the best-fitting parameter value. Using the same method, we checked the quality of the determination of the host parameters by starting the MCS host modeling routine with initial parameters, which progressively departs from the parameter set we found during the first modeling of each object. This enabled us to also check the stability of the solution found.

This procedure allowed us to distinguish three cases that we related to a quality criterion (Col. (9) in Table 2). The first, called 1, accounts for situations where the modeling algorithm converges towards similar solutions, whatever the starting point used, then giving reliable host parameters. The second, noted 2, corresponds to the cases where the solution strongly depends upon the initial parameters (generally corresponding to the faintest/rounder hosts). The last one, noted 3, is attributed to the cases where we detect no host-galaxy after the PSF-subtraction step.

We also considered among our sample of *new* PA_host *data* five objects that already had a PA_host determined in the literature. We find good agreement[4] between the previously published parameters and the one we derived, thereby assessing the capability of the method used in our study to recover host-galaxy parameters. This is not a surprise since the crucial step in the PA_host determination essentially lies in the proper subtraction of the quasar nucleus, a step carefully carried out for each of the objects in our compilation (see Sect. 2). Finally we also carried out simple ellipse fitting on the nuclear-subtracted images and observed that the derived PA_host agree (within $10°$) with those derived using the 2D profile-fitting procedure described in Sect. 3.1.2. On the other hand, the axial ratio b/a is more sensitive to the PSF subtraction and then not reliable enough to be used in the study. Therefore, in the following, we only use b/a to cut the sample (cf. Sect. 5).

4. Polarimetric and radio data

4.1. The polarimetric data

Most polarimetric data (the degree of polarization P and the polarization angle θ_{Pola}) were taken from a compilation of

---

[4] We find ΔPA_host within $10°$ for the class 1 quality objects, see Appendix B for more details.

Table 2. Results of our modeling of quasar host-galaxy.

Name	z	QSO type	Survey	Domain	Host type	b/a	PA$_{host}$	Quality
2M 000810+1354	0.185	RQ	Ma03	Vis	S	0.62	137	1
PG 0026+129	0.142	RQ	Ml01	NIR	E	0.86	113	1
PG 0043+039	0.385	RQ	Bo98	Vis	U	1.00	45	2
2M 005055+2933	0.136	RQ	Ma03	Vis	S	0.34	56	1
PG 0052+251	0.154	RQ	Ba97	Vis	S	0.70	171	1
PHL 909	0.171	RQ	Ba97	Vis	E	0.51	129	1
2M 010607+2603	0.411	RQ	Ma03	Vis	S?	0.31	115	1
SDSS J0123+0044	0.399	RQ	Za06	Vis	E	0.59	70	1
UM 357	0.335	RQ	Ml01	NIR	E	0.75	62	1
2M 015721+1712	0.213	RQ	Ma03	Vis	U	1.00	65	2
PKS 0202-76	0.389	RL	Bo98	Vis	...	...	...	3
NAB 0205+02	0.155	RQ	Ba97	Vis	S	0.67	140	1
2M 022150+1327	0.140	RQ	Ma03	Vis	S?	0.62	142	1
2M 023430+2438	0.310	RQ	Ma03	Vis	...	...	...	3
0316-346	0.265	RQ	Ba97	Vis	...	1.00	90	2
2M 032458+1748	0.328	RQ	Ma03	Vis	...	...	...	3
2M 034857+1255	0.210	RQ	Ma03	Vis	U	1.00	104	2
PKS 0440-00	0.844	RL	Ku01	NIR	...	...	...	3
MS 07546+3928	0.096	RQ	Bo98	Vis	E	1.00	72	2
2M 092049+1903	0.156	RQ	Ma03	Vis	S	0.52	24	1
SDSS J0920+4531	0.402	RQ	Za06	Vis	E	0.55	160	1
PG 0947+396	0.206	RQ	Ml01	NIR	S	0.71	22	1
HE 1029-140	0.086	RQ	Ba97	Vis	E	0.81	144	1
SDSS J1039+6430	0.402	RQ	Za06	Vis	E	0.88	20	1
PG 1048+342	0.167	RQ	Ml01	NIR	S	0.65	94	1
SDSS J1106+0357	0.242	RQ	Za06	Vis	S	0.66	66	1
PG 1116+215	0.177	RQ	Ba97	Vis	E	0.81	65	1
PG 1121+422	0.234	RQ	Ml01	NIR	...	...	...	3
PG 1151+117	0.176	RQ	Ml01	NIR	E	0.87	149	1
PG 1202+281	0.165	RQ	Ba97	Vis	E	0.92	117	1
PG 1216+069	0.334	RQ	Bo98	Vis	...	...	...	3
3C 273	0.158	RL	Ba97	Vis	E	0.79	61	1
2M 125807+2329	0.259	RQ	Ma03	Vis	E	0.72	61	1
PG 1307+085	0.155	RQ	Ba97	Vis	U	1.00	105	2
2M 130700+2338	0.275	RQ	Ma03	Vis	E	0.82	178	1
PG 1309+355	0.184	RQ	Ba97	Vis	S	0.82	3	1
PG 1322+659	0.168	RQ	Ml01	NIR	...	...	...	3
SDSS J1323-0159	0.350	RQ	Za06	Vis	E	0.71	26	1
PG 1352+183	0.158	RQ	Ml01	NIR	E	1.00	139	2
PG 1354+213	0.300	RQ	Ml01	NIR	E	0.78	166	1
PG 1358+043	0.427	RQ	Bo98	Vis	...	...	...	3
PG 1402+261	0.164	RQ	Ba97	Vis	S	0.61	170	1
SDSS J1413-0142	0.380	RQ	Za06	Vis	E	0.68	26	1
PG 1427+480	0.221	RQ	Ml01	NIR	E	1.00	158	2
PG 1444+407	0.267	RQ	Ba97	Vis	S	0.82	48	1
2M 145331+1353	0.139	RQ	Ma03	Vis	S	0.57	179	1
2M 151621+2259	0.190	RQ	Ma03	Vis	S	0.51	47	1
2M 152151+2251	0.287	RQ	Ma03	Vis	U	1.00	2	2
2M 154307+1937	0.228	RQ	Ma03	Vis	U	0.82	30	1
3C 323.1	0.266	RL	Ba97	Vis	E	0.76	99	1
NAB 1612+26	0.395	RQ	Ml01	NIR	E	0.55	99	1
Mrk 876	0.129	RQ	Ml01	NIR	U	1.00	131	2
2M 163700+2221	0.211	RQ	Ma03	Vis	S	0.29	121	1
2M 163736+2543	0.277	RQ	Ma03	Vis	U	1.00	128	2
2M 165939+1834	0.170	RQ	Ma03	Vis	U	0.81	61	1
2M 170003+2118	0.596	RQ	Ma03	Vis	...	...	...	3
2M 171442+2602	0.163	RQ	Ma03	Vis	S	0.59	169	1

measurements from the literature (Hutsemékers et al. 2005, and references therein). The polarimetric measurements for the objects of the sample of *Za06* have been published in their paper. For the 2-MASS reddened objects of the *Ma03* sample, the polarimetric data were taken from Smith et al. (2002). From this compilation we only considered and used data for objects where significant polarization is detected (i.e. such that $P/\sigma_P \geq 2$).

This also ensures that we only select data for which the the polarization angle is known with an uncertainty of $\sigma_{\theta_{Pola}} \leq 14°$.

4.2. The radio data

For each of the objects in our compilation that possess a PA$_{host}$ and a θ_{Pola}, we searched in the literature for radio data. The

Table 2. continued.

Name	z	QSO type	Survey	Domain	Host type	b/a	PA_{host}	Quality
2M 171559+2807	0.524	RQ	*Ma03*	Vis		1.00		2
KUV 18217+6419	0.297	RQ	*Ml01*	NIR	S?	1.00	65	2
3C 422	0.942	RL	*Ku01*	NIR	...	...	...	3
B2-2156+29	1.759	RL	*Ku01*	NIR	...	...	...	3
2M 222202+1959	0.211	RQ	*Ma03*	Vis	E?	1.00	46	2
2M 222554+1958	0.147	RQ	*Ma03*	Vis	S	0.49	141	1
PG 2233+134	0.325	RQ	*Ml01*	NIR	E	1.00	135	2
2M 225902+1246	0.199	RQ	*Ma03*	Vis	E	0.68	69	1
2M 230304+1624	0.289	RQ	*Ma03*	Vis	U	1.00	50	2
2M 230442+2706	0.237	RQ	*Ma03*	Vis	E	0.77	60	1
2M 232745+1624	0.364	RQ	*Ma03*	Vis	S	0.62	76	1
2M 234449+1221	0.199	RQ	*Ma03*	Vis	...	...	...	3
SDSS J2358-0009	0.402	RQ	*Za06*	Vis	U	1.00	68	2
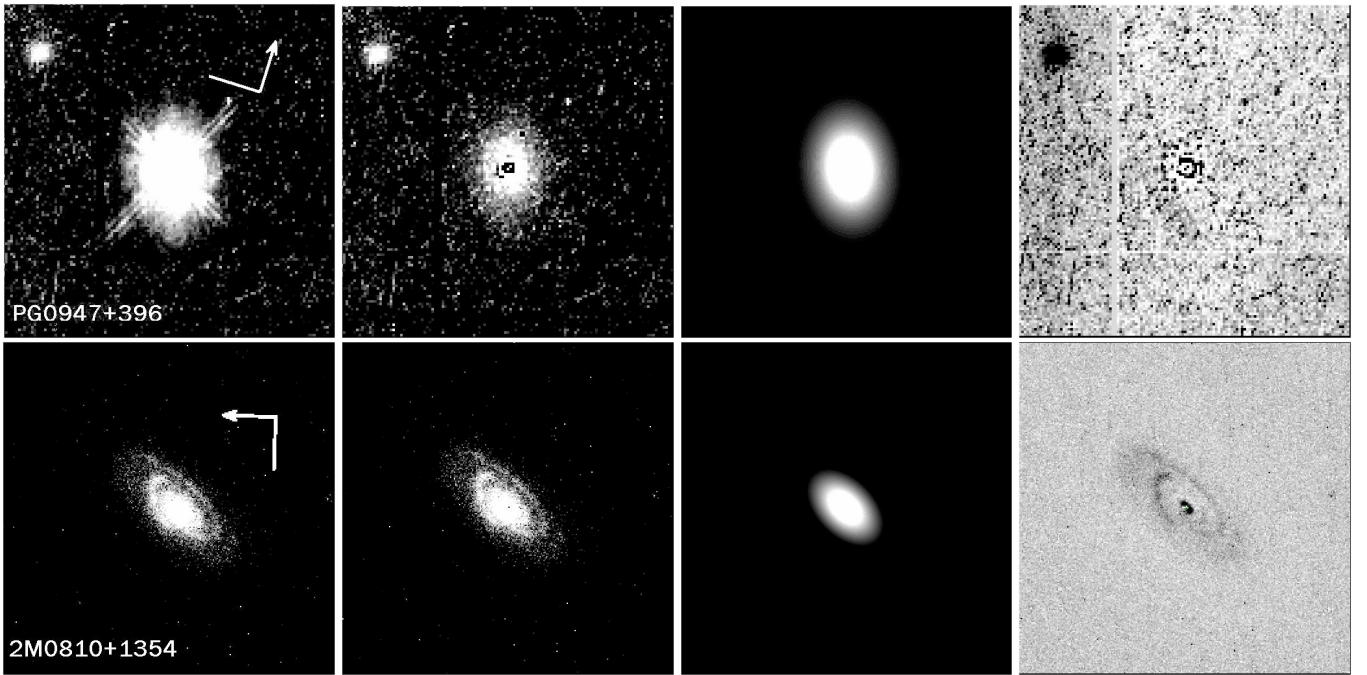
Fig. 1. Typical image analysis process and results for two representative objects in our sample (see text for details). North and east are marked on the left most frames (with the arrow pointing to the north). The top series of images presents one of the RQQs observed in the near-IR domain by *Ml01*: PG 0947+396. It shows that the PSF subtraction step is of prime importance characterizing the faint underlying host. The bottom series present the WFPC2 imaged 2M 000810+1354 RQQ by *Ma03*, hosted in a spiral galaxy.

radio data, referring to the RLQs, consists of radio-jet position angles PA_{Radio} determined on the basis of published Very Large Array (VLA) maps from the literature. The position angle PA_{Radio} refers to the orientation defined by the axis of the prominent jet (when seen); otherwise, it is the position angle of the large-scale radio morphology (brightest hotspot, outer lobes) relative to the core. As for the optical and near-IR PA_{host}, the angles are computed in degrees east of north.

A large part of the type 1 RLQ radio data come from the measurements realized by *Le99*. Other type 1 RLQ radio-jet data were found in the literature for several quasars (Table 3). In the case of the type 2 RLQs, the data come from the papers of *Ci93*, *Dk96*, and *Ma99* and essentially consist in compilations of VLA/Multi Element Radio Linked Interferometer Network (MERLIN) survey measurements from the literature.

5. Search for correlations

Table 6 with all data is available on-line. For the analysis, we selected the objects for which the data are relevant and accurate. Let us quickly summarize the criteria we used.

1. We have not considered Seyfert galaxies in this study. To avoid these objects, we only consider objects with $M_V \lesssim -23$ in the Véron catalogue version 12 (Véron-Cetty & Véron 2006). Two objects (0204+292 (*Du03*, $M_V = -22.4$) and 2344+184 (*Du03*, $M_V = -22.0$)) are then excluded from our sample. Two objects on the borderline (1635+119 (*Du03*, $M_V = -22.8$) and 0906+430 (*Le99*, $M_V = -22.9$)) are kept. This $M_V \lesssim -23$ criterion cannot be crudely applied to the reddened objets of *Ma03* and the type 2 radio-quiet objects of *Za06* since the luminosity of those objects is attenuated in the V-band. However, their high luminosity in the K-band or

Table 3. Radio data for the type 1 RLQs of our compilation which possess known PA$_{host}$ and θ_{Pola}.

Name (B1950)	Catalog name	z	PA$_{Radio}$[a] (°)	Reference[b]
0133+207	3C 47.0	0.425	35	Le99
0137+012	4C 01.04	0.258	30	5, 6, 7
0340+048	3C 393.0	0.357	40	Le99
0518+165	3C 138.0	0.759	70	Le99
0538+498	3C 147.0	0.545	60	Le99
0710+118	3C 175.0	0.770	60	Le99
0723+679	3C 179.0	0.846	90	Le99
0740+380	3C 186.0	1.067	140	Le99
0758+143	3C 190.0	1.195	30	Le99
0906+430	3C 216.0	0.670	40	Le99
1020– 103	...	0.197	155	5, 9
1100+772	3C 249.1	0.311	100	Le99
1111+408	3C 254.0	0.736	110	Le99
1137+660	3C 263.0	0.646	110	Le99
1150+497	4C 49.22	0.334	15	4, 8
1226+023	3C 273.0	0.158	60	10
1250+568	3C 277.1	0.320	130	Le99
1302– 102	...	0.286	25	10
1416+067	3C 298.0	1.436	90	Le99
1458+718	3C 309.1	0.905	145	Le99
1545+210	3C 323.1	0.266	20	3, 9
1618+177	3C 334.0	0.555	140	Le99
1704+608	3C 351.0	0.371	40	1, 2, 4
1828+487	3C 380.0	0.692	135	Le99
2120+168	3C 432.0	1.785	135	Le99
2135– 147	...	0.200	100	9
2247+140	4C 14.82	0.237	35	5

[a] PA$_{Radio}$ measured in degrees East of North. [b] References. (1) Bridle et al. (1994); (2) Price et al. (1993); (3) Bogers et al. (1994); (4) Reid et al. (1995); (5) Lister et al. (1994); (6) Hintzen et al. (1983); (7) Gower & Hutchings (1984a); (8) Owen & Pushell (1984); (9) Gower & Hutchings (1984b); (10) Readhead et al. (1979).

Table 4. Results of the two sample Kolmogorov-Smirnov test applied to the $\Delta\theta$ distribution of type 1 and type 2 quasars.

Selected sample[a]	N_1[b]	N_2[c]	P_{K-S}[d] (%)
RQ	24	5	7.24
RQ ($P \geq 0.6\%$)	15	5	15.75
RQ ($z \geq 0.2$)	8	5	0.11
RQ ($P \geq 0.6\%$ & $z \geq 0.2$)	5	5	0.37
RL	16	16	2.30
RL ($P \geq 0.6\%$)	14	15	1.95
RL ($z \geq 0.2$)	13	10	0.23
RL ($P \geq 0.6\%$ & $z \geq 0.2$)	13	10	0.23
RQ+RL	40	21	0.24
RQ+RL ($P \geq 0.6\%$)	29	20	0.21
RQ+RL ($z \geq 0.2$)	21	15	0.01
RQ+RL ($P \geq 0.6\%$ & $z \geq 0.2$)	18	15	0.03

[a] Criteria used to define sub-samples. [b] Size of the selected type 1 subsample. [c] Size of the selected type 2 subsample. [d] Probability P_{K-S} (in percent) that the $\Delta\theta$ of type 1 and type 2 objects are selected from the same parent sample.

in the [O III] emission lines testifies to their membership in the intrinsically luminous quasar sample.

2. We decided to fix an axial ratio limit $b/a < 0.9$ to eliminate the roundest host-galaxy morphology for which no accurate PA$_{host}$ determination could be obtained.
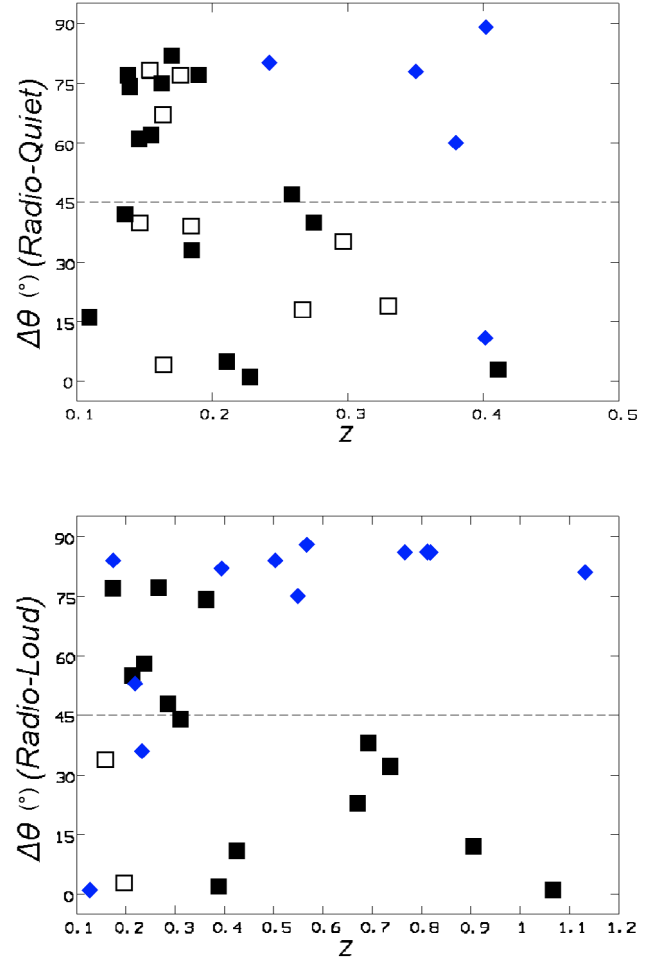
Fig. 2. Distribution of the acute angle $\Delta\theta$ between the polarization position angle θ_{Pola} and the orientation of the host-galaxy morphology PA$_{host}$, as a function of the redshift z. The upper panel refers to radio-quiet objects, while the lower panel refers to radio-loud objects. Type 1 objects are represented in both panel by squares and type 2 objects by diamonds. The filled symbols refer to objects with a polarization degree $P \geq 0.6\%$.

3. When several data were available for a given object parameter, we always selected the value with the smallest uncertainty.
4. For consistency, we always preferred data coming from larger homogeneous samples to those selected from smaller ones.

5.1. The PA$_{host}$ − θ_{Pola} correlation

Here we consider the host-galaxy data that were derived using observations taken in the visible domain ($\lambda_{obs} \sim 6000$ Å). The data obtained in the near-IR are discussed at the end of this section. We define $\Delta\theta$ as the acute angle between the polarization position angle θ_{Pola} and the host-galaxy orientation PA$_{host}$ in the visible: $\Delta\theta = 90 − |90 − |\theta_{Pola} − PA_{host}||$. Its value is defined between 0 and 90 degrees.

5.1.1. The radio-quiet objects

The upper panel of Fig. 2 summarizes the $\Delta\theta$ behavior as a function of the redshift for both type 1 and type 2 RQQ objects in

our sample. While at small redshifts, there seems to be no clear correlation between θ_{Pola} and PA_{host} for type 1 objects (the redshift extent of the type 2 RQQ sample is too limited to conclude), a distinct separation between the type 1 and type 2 behavior is noted for objects lying at higher redshifts ($z \gtrsim 0.2$–0.3) where the polarization direction of type 1 objects tends to be parallel to the host major axis ("alignment": $\Delta\theta \leq 45°$) while the polarization is mostly perpendicular to the host major axis in type 2 quasars ("anti-alignment": $\Delta\theta \geq 45°$). We also observe this type of behavior if we only consider the more polarized objects ($P \geq 0.6\%$ pictured by filled symbols). It is worth noting that the 2MASS reddened quasars from the *Ma03* study tend to appear at low $\Delta\theta$ values ($\Delta\theta \leq 45°$) like other un-reddened type 1 objects from the sample. We finally note that one type 2 RQQ quasar at $z = 0.402$ appears at low $\Delta\theta$. The behavior of this object, SDSS J0920+4531, already discussed in *Za06*, seems to be due to an unfortunate apparent superposition of a close companion galaxy leading to a biased PA_{host} determination.

To assess the significance of the alignment observed in the upper panel of Fig. 2, we carried out statistical tests on the type 1 and type 2 RQQ samples. We used the two-sample non-parametric Kolmogorov-Smirnov ($K - S$) test to determine whether the type 1 and type 2 $\Delta\theta$ distributions are drawn from the same parent population. The results of the $K - S$ tests applied to the two aforementioned samples using several selection criteria are summarized in Table 4. From these results, we can note that, while accounting for the whole RQQ sample does not allow an effective distinction between the type 1 and type 2 parent sample, the selection of the higher redshift objects ($z \geq 0.2$) shows that the probability is only 0.11% that the difference in the $\Delta\theta$ behavior seen among the two samples is fortuitous. The same conclusions can be reached if we only consider the more polarized objects ($P \geq 0.6\%$) but with a weaker statistical significance because the selected sample becomes smaller.

We also investigated the variation in $\Delta\theta$ as a function of the redshift considering type 1 and type 2 objects separately. To this aim, we performed a non parametric *Kendall-τ* rank test on the type 1 RQQ sample to check the strength of the correlation between the alignment ($\Delta\theta$) and the redshift. This statistical test uses the relative order of ranks in a data set to determine the likelihood of a correlation. We found a 4% probability that the anti-correlation between the $\Delta\theta$ and the redshift is purely fortuitous in the case of the type 1 RQQ sample. We do not use this test on our type 2 RQQ sample given its limited redshift range.

5.1.2. The radio-loud objects

The $\Delta\theta$ relation is also studied in the case of the radio-loud sample. The lower panel of Fig. 2 illustrates the observed $\Delta\theta$ behavior in this case. Once again, the $\Delta\theta$ distribution is clearly non-random. A first look allows to see that the type 1 RLQs are preferentially found at small $\Delta\theta$ (i.e. alignment between the polarization angle and the major axis of the host). Type 2 objects often exhibit large offset angles, $\Delta\theta \geq 45°$, indicating an anti-alignment between the polarization angle and the host-galaxy position angle (Cimatti et al. 1993).

The lower panel of Fig. 2 suggests a dependence on $\Delta\theta$ as a function of the redshift as already noted for the type 2 RLQs (Cimatti et al. 1993). Indeed, at low redshift ($z \leq 0.2$), as in the radio-quiet case (upper panel of Fig. 2), we do not find any particular $\Delta\theta$ difference for either type 1 or type 2 objects, while at higher redshift ($z \geq 0.3$–0.4), we observe a clear separation of the $\Delta\theta$.

Statistical tests were carried out on the data in order to assess the strength of the (anti-)alignment. The results of a two sample $K - S$ test using several selection criteria applied to radio-loud objects are summarized in Table 4. The two sample $K - S$ test comparing the distribution of type 1 and type 2 $\Delta\theta$ on the whole RLQ sample shows that there is only a 2.3% probability that the $\Delta\theta$ of the two samples are selected from the same parent distribution. More selective criteria[5] ($z \geq 0.2$, $P \geq 0.6\%$ or both) on the RLQ sample reinforce the conclusion of the statistical test.

A *Kendall-τ* correlation test considering type 1 and type 2 objects separately was applied to the sample in order to investigate the redshift dependency of the $\Delta\theta$ distribution. For the type 1 RLQs, the result of the test shows that there is a 4% probability that the anti-correlation of the $\Delta\theta$ with the redshift is purely fortuitous, while the probability that the correlation is fortuitous is only of 0.2% for type 2 objects.

5.1.3. A global view

A global look at both panels of Fig. 2 suggests similar behavior by the type 1/type 2 quasars whatever their radio-loudness: at $z \geq 0.2$–0.3 the type 1 objects systematically lie at small $\Delta\theta$ with their polarization mainly parallel ($\Delta\theta \leq 45°$) to their morphological major axis, while the type 2 objects are found at a higher offset angle ($\Delta\theta \geq 45°$). These observations are supported by statistical tests carried out on the mixed RQQ and RLQ sample (Table 4). The *Kendall-τ* correlation test led to the conclusion that there is a 0.2% probability that the correlation between $\Delta\theta$ and z is purely fortuitous for the type 2 quasars and of 0.4% that the anti-correlation is fortuitous for type 1 objects.

To verify that the difference in the behavior of $\Delta\theta$ between type 1 and type 2 quasars actually corresponds to alignment and anti-alignment, respectively, we computed the mean value $\overline{\Delta\theta}$ of the $\Delta\theta$ for both samples at $z \geq 0.2$ separately and compared this value to the distribution of mean offset angles computed from simulated samples obtained by shuffling the PA_{host} among the objects. We found that the $\overline{\Delta\theta} = 31°$ (resp. $\overline{\Delta\theta} = 72°$) value measured for the type 1 (resp. type 2) quasars has a probability of 0.3% (resp. 0.02%) of occuring in a random distribution of polarization and host position angles. This test was not applied to RQQ and RLQ samples separately given the small number of objects.

We also investigated the $PA_{host} - \theta_{Pola}$ correlation for the RQQ and RLQ samples using the compilation of near-IR PA_{host} data. However, for those data, we do not see any clear correlations between the polarization angle and the host-galaxy position angle even at higher redshifts ($z \geq 0.2$–0.3). This lack of correlation was confirmed by the $K - S$ and *Kendall-τ* tests.

5.2. Other interesting correlations

5.2.1. The $PA_{Radio} - \theta_{Pola}$ correlation

Using the available VLA radio-jet orientation for the radio-loud objects of our sample possessing optical polarization measurements (Table 3 and *Ci93*), we also investigate the $PA_{Radio} - \theta_{Pola}$ correlation. We define the radio-jet/polarization offset angle in

---

[5] Although the alignment/anti-alignment seems to appear at higher redshift for RLQs, we keep the cutoff in the test at $z \geq 0.2$ for consistency with RQQs. However, using a higher redshift cutoff results in even more significant correlations.
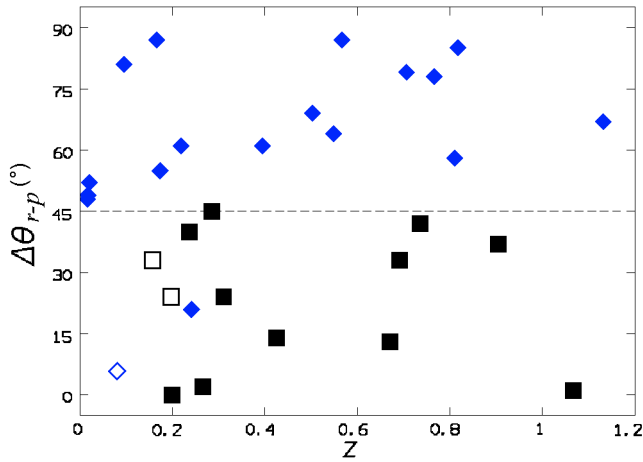
Fig. 3. Distribution of the acute angle $\Delta\theta_{r-p}$ between the polarization position angle θ_{Pola} and the orientation of the radio jet PA_{Radio} defined in Sect. 4.2. As in the other figures, type 1 objects are represented by squares and type 2 objects are represented by diamonds. The symbols are filled when $P \geq 0.6\%$.

the same way as the offset defined in Sect. 5.1: $\Delta\theta_{r-p} = 90 - |90 - |\theta_{Pola} - PA_{Radio}||$, whose value is between 0 and 90 degrees.

Figure 3 synthesizes the $\Delta\theta_{r-p}$ distribution for the radio-loud objects as a function of the redshift. One can note that the radio-jet of type 1 RLQs are mostly aligned with the polarization ($\Delta\theta_{r-p} \leq 45°$), while these two directions are mostly anti-aligned in type 2 objects ($\Delta\theta_{r-p} \geq 45°$). Moreover, we do not see any redshift dependence of the correlation. We carry out $K - S$ test over the $\Delta\theta_{r-p}$ distribution of type 1 and type 2 objects. The two sample $K - S$ test shows that there is less than a 0.001% probability that both samples are selected from the same parent distribution. This result is even more significant if we only consider the $P \geq 0.6\%$ quasars. We also find a 0.17% (resp. 0.06%) probability that the $\overline{\Delta\theta_{r-p}} = 24°$ measured for type 1 RLQs (resp. $\overline{\Delta\theta_{r-p}} = 65°$ for type 2) comes from a random $\Delta\theta_{r-p}$ distribution.

These (anti-)alignment effects were already reported previously in the literature. For the type 1 objects, a clearly non-random distribution of $\Delta\theta_{r-p}$ has been reported by many authors (e.g. Stockman et al. 1979; Rusk & Seaquist 1985; Berriman et al. 1990; Lister & Smith 2000), showing that the optical polarization angle of type 1 RLQs mostly aligns with their radio-morphology. For the type 2 RLQs the anti-alignment between the radio-jets and the optical polarization is known as part of the so called "*RG alignment effect*" observed in high-z radio galaxies (e.g. McCarthy et al. 1987; Chambers et al. 1987; Cimatti et al. 1993). Indeed, using polarization measurements and VLA radio observations of RGs, they found a strong anti-alignment between the linear polarization orientation and the radio structure.

5.2.2. The $PA_{Radio} - PA_{host}$ correlation

Using the radio-jet orientations given in Table 3 and *Ci93* for the radio-loud objects of our sample with a reliable host-galaxy position angle, we finally look at the correlation of the radio-jet with the morphology of the host. We define the offset angle $\Delta\theta_{r-o}$ between the radio-jet and host major axis position angle using the same definition as in the preceding sections. Figure 4 summarizes the behavior of $\Delta\theta_{r-o}$ as a function of the redshift.
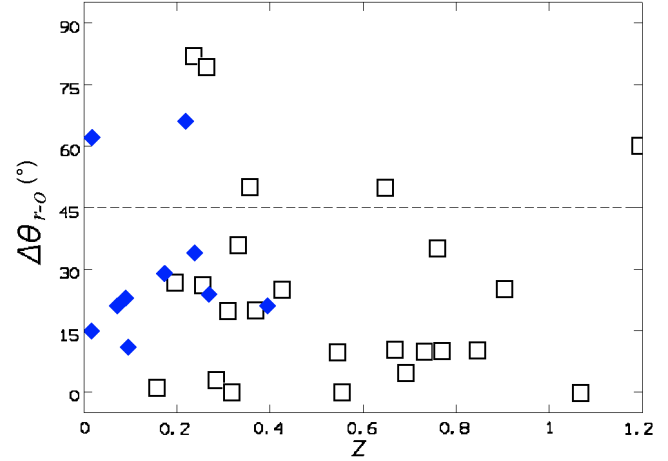

Fig. 4. Distribution of the acute angle $\Delta\theta_{r-o}$ between the orientation of the radio jet PA_{Radio} and the host-galaxy position angle PA_{host} in the visible domain. Type 1 objects are represented by empty squares and type 2 objects are represented by filled diamonds.

Table 5. Summary of the correlations studied.

Radio type	Correlation	type 1[a]	type 2[a]
RQ	$PA_{host} - \theta_{Pola}$	$\parallel^{(6)}$	$\perp^{(5)}$
RL	$PA_{host} - \theta_{Pola}$	$\parallel^{(6)}$	$\perp^{(1)}$
RL	$\theta_{Pola} - PA_{Radio}$	$\parallel^{(3)}$	$\perp^{(1)}$
RL	$PA_{host} - PA_{Radio}$	$\parallel^{(2,6)}$	$\parallel^{(1,4)}$

[a] Numbers in parentheses give the reference to the first detection of a given correlation for type 1 and type 2 quasars : (1) Chambers et al. (1987); McCarthy et al. (1987); Cimatti et al. (1993); (2) *Le99*; (3) Stockman et al. (1979); (4) Biretta et al. (2002); (5) Zakamska et al. (2006) and (6) this work.

For the type 1 RLQs, we note a significant alignment ($P \leq 0.001\%$ that the measured $\overline{\Delta\theta_{r-o}} = 24°$ is due to chance) between the host-galaxy's main orientation and the radio-jet orientation, as first reported within a larger sample in *Le99*. This is not a surprise, since 2/3 of the type 1 RLQ sample used to check this correlation is built on the measurements given in *Le99*.

For the type 2 RLQs (the NLRGs), we also note an alignment ($\Delta\theta_{r-o} \leq 45°$) between the radio-jet and the host position angle. The permutation test gives a $P \leq 8\%$ that the measured $\overline{\Delta\theta_{r-o}} = 30°$ is due to chance. Although one might suspect a redshift dependence on Fig. 4, it is not significant in our sample (as the result of the *Kendall-τ* test). Let us notice that this alignment is known as part of the "*RG alignment effect*" (e.g. McCarthy et al. 1987; Chambers et al. 1987) where the optical morphology of higher redshift ($z \geq 0.5$) RGs aligns with the radio-jet.

5.3. Summary of the results

The known correlations between quasar orientation parameters are summarized in Table 5. The main result of our study is the discovery of a correlation between PA_{host} and θ_{Pola} in quasars observed whatever their radio-loudness but depending on the spectroscopic type of the source. We find that, while high-redshift type 2 quasars exhibit an anti-alignment of their optical polarization angle with their optical, rest frame UV/blue, morphology, the optical host galaxy position angle tends to be aligned with the polarization angle in type 1 quasars.

Another interesting result is the redshift dependence of the alignment. Indeed, as suggested by both upper and lower panels of Fig. 2 and the results of the statistical tests, the alignment becomes significant if we consider redshifts higher than $z \sim 0.2-0.3$ for either radio-loud or radio-quiet objects. This observation may explain the lack of correlation observed by Berriman et al. (1990) between θ_{Pola} and PA_{host} since the redshift extent of their sample was rather small (among their 24 objects with $z \leq 0.4$, only 5 of them have $z \geq 0.3$). Note that the precise cutoff is not clearly determined and might be slightly higher, as suggested by RLQs (Fig. 2). Observations of RQQs at higher z would be needed to clarify this point.

Finally, we note that, while the alignment between the host-galaxy position angle and the polarization angle is clearly observed and statistically significant in the case of the optical PA_{host} data, we do not find similar behavior with the near-IR PA_{host} data. Optical and K-band studies of high z RGs have already shown that, while an alignment effect is observed between their optical emission and their radio axis, a significantly weaker alignment is observed between the K-band emission and the radio axis (Rigler et al. 1992; Dunlop & Peacock 1993; Best et al. 1998). This argues in favor of a scheme where the K-band emission is not necessarily related to the visible (rest-frame blue) light.

6. Discussion

6.1. The observed correlation

In Sect. 5 we reported on the existence of an (anti-)alignment between the linear polarization and the host-galaxy position angle of (type 2) type 1 quasars. We noticed that this behavior seems to be independent of the radio-loudness. It is also interesting to recall the lack of correlation in the near-IR domain and the redshift dependence of the $PA_{\text{host}} - \theta_{\text{Pola}}$ (anti-)alignment. These last two facts lead us to think that the observed correlations might be linked to the rest-frame UV/blue part of the quasar light, which is redshifted to optical wavelengths for the higher z objects. This hypothesis is supported by Fig. 5, where we plot $\Delta\theta$ as a function of λ_{rest}, the rest-frame wavelength at which PA_{host} is measured (i.e. the central wavelength of the imaging filter divided by $1 + z$).

We note that, while at longer wavelengths there is no particular behavior in the $\Delta\theta$ distribution for either type 1 or type 2 objects, the (anti-)alignment effect clearly appears at shorter wavelengths ($\lambda_{\text{rest}} \lesssim 5000$ Å). At $\lambda_{\text{rest}} \leq 5000$ Å, a two-sample $K - S$ test shows that there is a 0.01% probability that the $\Delta\theta$ distribution of type 1 and type 2 quasars is drawn from the same parent sample.

6.2. The UV/blue continuum and the origin of the correlation

The morphology of type 2 radio-loud objects (NLRGs) has been extensively studied in the literature since those objects do not possess a bright central nucleus masking the underlying host, and they can be observed at high redshifts. Imaged at optical wavelengths, higher redshift RGs ($z \geq 0.5$) are known to show the aforementioned "*RG alignment effect*" where the extended rest-frame UV/blue continuum emission aligns with the radio jet. This alignment, not seen in the near-IR images of the same objects (Rigler et al. 1992), leads to a two-component RG model: at shorter wavelengths, the continuum is dominated by an extended UV/blue component aligned with the radio axis, while at longer wavelengths, the quasar light is dominated by a stellar
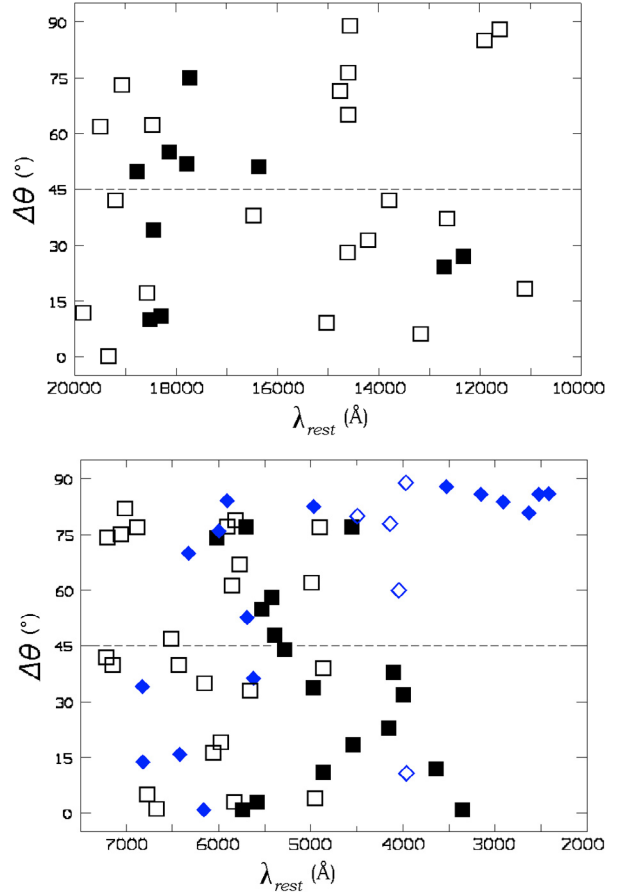

Fig. 5. Distribution for RQQs and RLQs of the acute angle $\Delta\theta$ between PA_{host} and θ_{Pola} as a function of the observation wavelength λ_{rest} as measured in the quasar rest-frame. The upper panel presents the $\Delta\theta$ distribution at near-IR wavelengths, while the lower panel presents the same distribution at UV/visible wavelengths. RQQs are represented by empty symbols and RLQs by filled symbols. Type 1 objects are pictured by squares and type 2 objects by diamonds. No observations of type 2 quasars are available in the near-IR. Our sample does not contain quasars imaged at 7500 Å $\leq \lambda_{\text{rest}} \leq 11\,000$ Å.

component that possesses the morphology and physical dimensions of elliptical galaxies.

This extended UV/blue continuum, which can show quite a complex morphology (McCarthy et al. 1997), was primarily interpreted, given its alignment with the radio-jet, as massive star formation regions triggered by the shocks associated to the passage of the radio-jet through the host-galaxy (McCarthy et al. 1987). However, as we briefly recall in Sect. 5.1.2, high-redshift NLRGs are also known to show an anti-alignment between their optical linear polarization and their rest frame UV/blue morphological structure (e.g. Cimatti et al. 1993; Hurt et al. 1999), supporting the possibility that at least part of this extended UV/blue light is due to the polar scattering of the light from the quasar nucleus by electrons and/or dust (di Serego Alighieri et al. 1989; Cimatti et al. 1993; di Serego Alighieri et al. 1993; Dey et al. 1996; Tadhunter et al. 2002). Indeed, this assumption provides a simple explanation of the fact that the polarization angle is perpendicular to the optical, extended rest-frame UV/blue light in the host-galaxy.

Because of their apparent faintness and the absence of strong radio counterpart, type 2 RQQs have long been searched for. The hard X-ray and SDSS surveys recently unveiled large

samples of type 2 RQQ candidates, showing that these objects are not extraordinarily rare (e.g. Zakamska et al. 2003 and references therein). The HST spectropolarimetric study of a sample of 12 type 2 RQQs revealed that a large part of them (9 out of 12) possess high optical polarization and that, for 5 objects, their polarized spectra contain broad emission lines betraying the presence of a type 1 nucleus (Zakamska et al. 2005). Three-band HST imaging of 9 type 2 RQQs also reveals some morphologically complex emission that appears in the bluer images (*Za06*). These structures were interpreted as scattering cones since their position angle lies almost perpendicular to the *E-vector* polarization plane. As in NLRGs, scattering in the extended UV/blue component seems to represent a viable interpretation of the origin of the detected polarization.

The detection of a hypothetical extended blue component in either RL or RQ type 1 quasars is hindered by the central source whose strong contribution at smaller wavelengths remains difficult to estimate and properly subtract. However, if type 1 and type 2 objects are, according to the unification model, intrinsically identical, the extended scattering region resolved in type 2 quasars should also be present, but masked by the higher apparent brightness of the unobscured central source. Since the viewing angle of type 1 and type 2 objects is thought to be an essential parameter controlling the observed properties of those objects, the polarization geometry may also be affected by the viewing angle. While type 2 objects are almost seen edge-on in this framework such that the extended polar scattering regions produce a polarization angle perpendicular to the symmetry axis of the AGN (pictured by the radio-jet axis in the RLQ objects), the situation may be different in the nearly face-on type 1 quasars.

An enticing interpretation of the polarization properties has recently been proposed for the Seyfert galaxies. Indeed, Seyfert galaxies exhibit some kind of *alignment effect* between their optical linear polarization and their radio axis. While the type 2 objects polarization is known to be anti-aligned with the radio axis (Antonucci 1983), the polarization originating from scattering cones perpendicular to the obscuring torus (Antonucci & Miller 1985), type 1 Seyferts are found to be of both kinds (aligned and anti-aligned, Smith et al. 2002). The scenario proposed to account for these observations consists of a two-component polar+equatorial scattering model (Smith et al. 2004, 2005; Goosmann et al. 2007). While the extended polar-scattering region accounts for the perpendicular polarization, the much smaller equatorial disk-like component inside the obscuring torus produces a polarization that, projected onto the plane of the sky, is parallel to the symmetry axis of the system (see Fig. 6). In this framework, type 2 polarization properties are dominated by polar scattering, the equatorial component being hidden by the dusty torus. In type 1 objects, the smaller but significantly non-zero inclination angle of the system is such that both scattering regions contribute to the polarized flux, where the resulting polarization is dominated by the equatorial scattering component (Smith et al. 2002).

This two-component scattering scheme seems to fit our observations nicely as it provides an explanation for the correlations found in Sect. 5.1 assuming that the observed polarization is due to scattering (in both RQ and RL objects) and that the morphology of the host-galaxy/extended emission observed in higher redshift quasars is, at least in part, related to scattered UV/blue light[6]. The model also provides a simple explanation

---

[6] Let us emphasize that only the polar scattering region – assumed to be parallel to the symmetry axis of the system – can be angularly resolved (in principle in both type 1 and type 2 objects). The equatorial
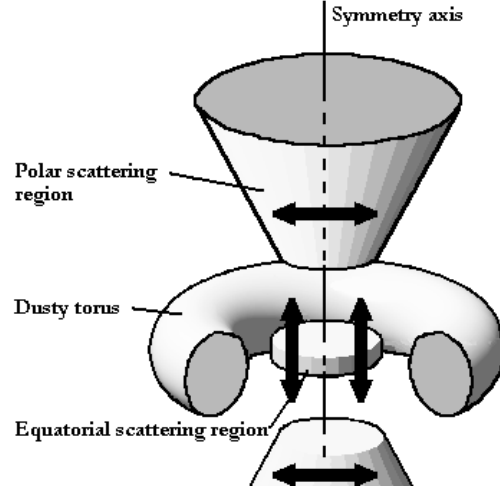

Fig. 6. Cartoon illustrating the adopted quasar model, and more particularly, the two scattering regions used to interpret our results (adapted from Smith et al. 2004). The system is shown inclined with respect to the line of sight to the observer such that a type 1 object is seen. In type 2 objects the dusty torus is seen edge-on and the central part is hidden. The arrows indicate the direction of the resulting polarization projected onto the plane of the sky for each scattering region (see text for more details). In RLQs, the radio jet (not illustrated) extends along the symmetry axis.

of the alignment seen in type 1 and type 2 RLQs between their polarization position angle and their radio jets, since the radio jets are thought to be emitted along the symmetry axis of the accretion disk, which also defines the direction of the extension of the polar scattering regions. Moreover, assuming the proposed model applies and recalling the lack of correlation in the near-IR (which samples the stellar component), our observations suggest that the central engine symmetry axis and the orientation of the stellar component are not correlated. This lack of correlation has already been reported in the case of Seyfert and radio galaxies (e.g. Kinney et al. 2000, and references therein; Schmitt et al. 2001) suggesting alternative models to the fuelling of the AGN supermassive black hole (e.g. King & Pringle 2007). Our results suggest that such scenarii might also apply to the higher luminosity quasars.

Recent HST two-band imaging of type 1 RQQs (e.g. Sanchez et al. 2004; Jahnke et al. 2004) shows an enhancement of the rest-frame blue light of the host-galaxy with respect to normal galaxies of similar redshift and luminosity. This blue excess is actually explained as due to merger-induced activity. However, those objects do not show more evidence of interaction than inactive galaxies at similar redshift and luminosity (Sanchez et al. 2004). Polarimetric study of these objects might provide an explanation of this excess blue light in terms of scattering, although an accurate estimate of the fraction of scattered light in type 1 quasars might be difficult given the fact that the observed polarization is the combination of both polar and equatorial polarization acting in opposite ways.

Let us finally note that we also searched – without success – for a possible correlation between $\Delta\theta$ and the quasar absolute magnitude, since the fraction of scattered over stellar light may

---

scattering region -perpendicular to the symmetry axis- is too small to be resolved. Note that, in this framework, given the projections effects and the presence of two competing scattering regions, we expect the dispersion of the $\Delta\theta$ to be higher for type 1 quasars than for type 2 ones as it might be suspected in Fig. 2.

be more important in the hosts of intrinsically more luminous quasars.

7. Conclusions

Using host-galaxy position angles (PA_{host}) determined from high-resolution optical/near-IR images of quasars and data from the literature, we investigated the possible existence of a correlation between the host morphology and the polarization direction in the case of RQQs and RLQs. We can summarize our results as follows:

1. We find an alignment between the direction of the linear polarization and the rest-frame UV/blue major axis of the host-galaxy of type 1 quasars. In the case of type 2 objects, it is well-established that the extended UV/blue light is correlated to the observed polarization, as these blue regions are thought to be dominated by scattering. Our results suggest that such an extended UV/blue scattering region is also present in type 1 quasars.
2. We do not find such an alignment effect with the near-IR host morphology. This suggests that the morphology of the extended UV/blue emission is not related to the morphology of the stellar component of the host-galaxy that dominates in the near-IR.
3. We observe the same $PA_{host} - \theta_{Pola}$ behavior for either radio-loud or radio-quiet objects. This observation supports the idea that the UV/blue continuum is not entirely due to star formation processes triggered by the radio jet.
4. The observed correlation fits a unification model where the type 1/type 2 dichotomy is essentially determined by orientation effects assuming the two-component scattering model of Smith et al. (2004, 2005). Indeed, depending on the viewing angle to the quasar, the polarization would predominantly arise from either the equatorial or the polar scattering region giving rise to the observed behavior.

In order to strengthen the conclusions and to investigate the correlations presented in this paper further, new observations of quasars in the rest-frame UV/blue domain are needed, especially of radio-quiet objects for which few observations at $\lambda_{rest} \leq 5000$ Å are available. The detection of the extended blue/UV continuum region and the measurement of its polarization would help for testing our interpretation.

References

Antonucci, R. 1983, Nature, 303, 158
Antonucci, R. 1993, ARA&A, 31, 473
Antonucci, R., & Miller, J. 1985, ApJ, 93, 785
Bagget, S., et al. 2002, WFPC2 Data Handbook, version 4.0 (Baltimore : STScI)
Bahcall, J. N., Kirhakos, S., & Schneider, D. P. 1996, ApJ, 457, 557
Bahcall, J. N., Kirhakos, S., & Saxe, D. H. 1997, ApJ, 479, 642
Barthel, P. D. 1989, AJ, 336, 606

Berriman, G., Schmidt, G. D., West, S. C., & Stockman, H. S. 1990, ApJS, 74, 869
Best, P. N., Longair, M. S., & Röttgering, J. A. 1998, MNRAS, 295, 549
Biretta, J. A., Martel, A. R., McMaster, M., et al. 2002, New Astron. Rev., 46, 181
Bogers, W. J., Hes, R., Barthel, P. D., & Zensus, J. A. 1994, A&A, 105, 91
Boyce, P. J., Disney, M. J., Blades, J. C., et al. 1998, MNRAS, 298, 121
Bridle, A. H., Hough, D. H., Lonsdale, C. J., Burns, J. O., & Laing, R. A. 1994, AJ, 108, 766
Chambers, K. C., Miley, G. K., & van Breugel, W. 1987, Nature, 329, 604
Cimatti, A., di Serego-Alighieri, S., Fosbury, R. A. E., Salvati, M., & Taylor, D. 1993, MNRAS, 264, 421
Cohen, M. H., Ogle, P. M., Tran, H. D., Goodrich, R. W., & Miller, J. S. 1999, AJ, 118, 1963
de Koff, S., Baum, S. A., Sparks, W. B., et al. 1996, ApJS, 107, 621
Dey, A., Cimatti, A., van Breugel, W., Antonucci, R., & Spinrad, H. 1996, ApJ, 465, 157
di Serego Alighieri, S., & Fosbury, R. A. E. 1993, Quinn, P. J. & Tadhunter, C. N. 1989, Nature, 341, 307
di Serego Alighieri, S., Cimatti, A., & Fosbury, R. A. E. 1993, ApJ, 404, 584
Disney, M. J., Boyce, P. J., Blades, J. C., et al. 1995, Nature, 376, 150
Dunlop, J. S., & Peacock, J. A. 1993, MNRAS, 263, 936
Dunlop, J. S., McLure, R. J., Kukula, M. J., et al. 2003, MNRAS, 340, 1095
Floyd, D. J. E., Kukula, M. J., Dunlop, J. S., et al. 2004, MNRAS, 355, 196
Goosmann, R. W., & Gaskell, C. M. 2007, A&A, 465, 129
Gower, A. C., & Hutchings, J. B. 1984a, PASP, 96, 19
Gower, A. C., & Hutchings, J. B. 1984b, AJ, 89,1658
Grandi, P., Malaguti, G., & Fiocchi, M. 2006, ApJ, 642, 113
Guyon, O., Sanders, B. D., & Stockton, A. 2006 [arXiv:astro-ph/0605079v1]
Haas, M., Siebenmorgen, R., Shultz, B., Krügel, E., & Chini, R. 2005, A&A, 442, L39
Hao, L., Strauss, M. A., Tremonti, C. A., et al. 2005, AJ, 129, 1783
Hintzen, P., Ulvestad, J., & Owen, F. 1983, AJ, 88, 709
Hurt, T., Antonucci, R., Cohen, R., Kinney, A., & Krolik, J. 1999, ApJ, 514, 579
Hutsemékers, D., Cabanac, R., Lamy, H. & Sluse, D. 2005, A&A, 441, 915
Jackson, N., & Rawlings, S. 1997, MNRAS, 286, 241
Janhke, K., Sanchez, S. F., Wisotzki, L., et al. 2004, AJ, 614, 568
Kellerman, K. I., Sramek, R., Schmidt, M., Shaffer, D. B., & Green, R. 1989, AJ, 98, 1195
King, A. R., & Pringle, J. E. 2007, MNRAS, 377, L25
Kinney, A. L., Schmitt, H. R., Clarke, C. J., et al. 2000, ApJ, 537, 152
Koekemoer, A. M., Fruchter, A. S., Hook, R. N., & Hack, W. 2002, HST Calibration Workshop, ed. S. Arribas, A. M. Koekemoer, & B. Whitmore (Baltimore: STScI)
Kotilainen, J. K., & Falomo, R. 2004, A&A, 424, 107
Krist, J., & Hook., R. 2004, http://www.stsci.edu/software/tinytim
Kukula, M. J., Dunlop, J. S., McLure, R. J., et al. 2001, MNRAS, 326, 1533
Lawrence, A. 1987, PASP, 99, 309
Lehnert, M. D., Miley, G. K., Sparks, W. B., et al. 1999, ApJS, 123, 351
Lister, M. L., & Smith, P. S. 2000, AJ, 541, 66
Lister, M. L., Gower, A. C., & Hutchings, J. B. 1994, AJ, 108, 821
McCarthy, P. J., van Breugel, W. J. M., Spinrad, H., & Djrgovski, S. 1987, ApJ, 321, L29
McCarthy, P. J., Miley, G. K., de Koff, S., et al. 1997, ApJS, 112, 415
McLeod, K. K., & McLeod, B. A. 2001, ApJ, 546, 794
McLure, R. J., Kukula, M. J., Dunlop, J. S., et al. 1999, MNRAS, 308, 377
McLure, R. J., Dunlop, J. S., & Kukula, M. J. 2000, MNRAS, 318, 693
McLure, R. J., Willott, C. J., Jarvis, M. J., et al. 2004, MNRAS, 351, 347
Magain, P., Courbin, F., & Sohy, S. 1998, ApJ, 449, 472
Marble, A. R., Hines, D. C., Schmidt, G. D., et al. 2003, ApJ, 590, 707
Martel, A. R., Baum, S. A., Sparks, W. B., et al. 1999, ApJS, 121, 81
Owen, F. N., & Puschell, J. J. 1984, AJ, 89, 932
Pavlovsky, C., et al. 2005, ACS Data Handbook, version 4.0 (Baltimore : STScI)
Peng, C., Ho, L. C., Impey, C. D., & Rix, H.-W. 2002, AJ, 124, 266
Percival, W. J., Miller, L., McLure, R. J., & Dunlop, J. S. 2001, MNRAS, 322, 843
Phillipps, S., & Boyce, P. J. 1992, MNRAS, 256, 673
Pian, E., Falomo, R., Hartman, R. C., et al. 2002, A&A, 392, 407
Price, R., Gower, A. C., Hutchings, J. B., et al. 1993, ApJS, 86, 365
Readhead, A. C. S., Pearson, T. J., Cohen, M. H., Ewing, M. S., & Moffet, A. T. 1979, ApJ, 231, 299
Reid, A., Shone, D. L., Akujor, C. E., et al. 1995, A&A, 110, 213
Rigler, M. A., Lilly, S. J. Stockton, A., Hammer, F., & Le Fèvre, O. 1992, ApJ, 385, 61
Rudy, R. J., Schmidt, G. D., Stockman, H. S., & Moore, R. L. 1983, AJ, 271, 59
Rusk, R., & Seaquist, E. R. 1985, AJ, 90, 30
Sanchez, S. F., Jahnke, K., McIntosh, D. H., et al. 2004, ApJ, 614, 586

Schmidt, M., & Green, R. F. 1983, ApJ, 269, 352

Schmitt, H. R., Ulvestad, J. S., Kinney, A. L., et al. 2001, ASPC, 249, 230

Schultz, A., et al. 2005, NICMOS Instrument Handbook, version 8.0 (Baltimore: STScI)

Sérsic, J. L. 1968, Atlas de Galaxias Australes, Observatorio Astronomico, Córdoba

Siebenmorgen, R., Freudling, W., Krügel, E., & Haas, M. 2004, A&A, 421, 129

Smith, J. E., Young, S., Robinson, A., et al. 2002, MNRAS, 335, 773

Smith, J. E., Robinson, A., Alexander, et al. 2004, MNRAS, 350, 140

Smith, J. E., Robinson, A., Young, S., Axon, D. J., & Corbett, E. A. 2005, MNRAS, 359, 846

Smith, P. S., Schmidt, G. D., Hines, D. C., Cutri, R. M., & Nelson, B. O. 2002, ApJ, 569, 23

Spencer, R. E., Schilizzi, R. T., Fanti, C., et al. 1991, MNRAS, 250, 225

Stockman, H. S., Angel, R. J. P., & Miley, G. K. 1979, ApJ, 227, L55

Tadhunter, C. N., Morganti, R., Robinson, A., et al. 1998, MNRAS, 298, 1035

Tadhunter, C. N., Dickson, R., Morganti, R., et al. 2002, MNRAS, 330, 977

Taylor, G. L., Dunlop, J. S., Hughes, D. H., & Robson, I. E. 1996, MNRAS, 283, 930

Thompson, I. A., & Martin, P. G. 1988, ApJ, 330, 121

Urry, M. C., & Padovani, P. 1995, PASP, 107, 803

van Bemmel, I. M., & Bertoldi, F. 2001, A&A, 368, 414

Veilleux, S., Kim, D. C., Peng, C. Y., et al. 2006, ApJ, 643, 707

Véron-Cetty, M. P., & Véron, P. 2006, A&A, 455, 773

Zakamska, N. L., Strauss, M. A., Krolik, J. H., et al. 2003, AJ, 126, 2125

Zakamska, N. L., Schmidt, G. D., Smith, P. S., et al. 2005, AJ, 129, 1212

Zakamska, N. L., Strauss, M. A., Krolik, J. H., et al. 2006, AJ, 132, 1496

Online Material

Appendix A: details on the observation campaigns used in this study

In this Appendix, we give some details about each of the observing campaigns used in this study and briefly described in Sect. 2.

A.1. Sample of published and reliable data

A.1.1. The visible domain

Ci93 (Cimatti et al. 1993) The sample defined in *Ci93* consists in a compilation of $z \geq 0.1$ RGs studied in the literature, which possess polarization measurements in the optical domain. Their total sample was built from 42 RGs, from which 8 NLRGs have $z \in [0.5-1.2]$. NLRGs possess an obvious host orientation in their rest-frame UV/blue (redshifted to optical) continuum images (*Ci93* and references therein). The $\Delta\theta_O$ given in Table 1 of *Ci93* are the acute offset angle between the main orientation of their optical host image (our PA_{host}) and the optical polarization angle θ_{Pola}.

Di95 (Disney et al. 1995) The observations were made using the Planetary Camera (PC1) of the Wide Field & Planetary Camera2 (WFPC2, Bagget et al. 2002) on board the HST. The PC1 is a 800 X 800 pixel camera and has a 0.046 arcsec per pixel resolution. Four quasars whose redshift z belongs to [0.25, 0.50] were imaged through the broadband F702W filter (which corresponds roughly to R band). The host galaxies parameters were derived using a two-component cross-correlation technique that finds the best fit between the observed images and a series of galaxy templates (Phillipps & Boyce 1992).

Dk96 (de Koff et al. 1996) The sample presented here is part of a more extended sample, containing 267 3CR objects. In the sample of *Dk96*, 77 RGs at intermediate $(0.1 < z < 0.5)$ redshift were studied with the PC1 camera of the WFPC2 camera through the F702W filter. The host-galaxy PA_{host} was determined by hand on the images by measuring the position angle of the largest extensions of the emission regions at a given surface brightness. The uncertainty in the derived position angles may thus be as large as $15°$ depending on the complexity of the objects.

Le99 (Lehnnert et al. 1999) Forty-three RLQs selected from the 3CR radio catalog and spanning a redshift range of $z \in [0.3, 2.0]$ were imaged using the PC1 camera of the WFPC2 instrument on board the HST. The observations were carried out in the F702W filter. The PA_{host} were estimated by fitting a series of ellipses on the residuals after the substraction of a scaled point spread function (PSF) playing the role of the unresolved nucleus. Because the ellipticity of the isophotes for some objects can vary with radial distance to the center of the quasar, they defined the PA_{host} as the position angle of the major axis at a surface brightness of 21.5 m_{F702W} arcsec^{-2}. They estimated the uncertainty on the derived PA_{host} of less than $20°$ and an uncertainty of less than 0.07 on the ellipticity). Note that they do not provide b/a values in their Table 3, preventing us of using the b/a criterion for these objects. However, this is not a problem since no PA_{host} are provided for the objects with unreliable PA_{host} measurement. Moreover, we apply a redshift cut $(z < 1.20)$ in order to avoid the presence of tiny hosts for which the PA_{host} determination remains uncertain.

Ma99 (Martel et al. 1999) Forty-six 3CR radio galaxies were imaged thanks to the PC1 and the Wide Field (WF, the resolution of the WFs captors is $0.''0996$ pixel^{-1}) chips of the WFPC2 camera of HST through the F702W filter. The targets were selected so that their redshift belong in the range [0, 0.1]. They used the Vista command *axes* to calculate the flux-weighted position angle of the major axis and the ellipticity of the host-galaxy.

Du03 (Dunlop et al. 2003) For convenience, this sample gathers the published data by Dunlop et al. (2003) and McLure et al. (1999) under the same name because they are both taken from the same HST survey. Thirty-three objects (RQQs, RLQs and RGs) with $z \in [0.1, 0.25]$ were observed with the WF2 camera of the WFPC2 instrument through the F675W filter (corresponding roughly to R band). The parameters of the host galaxies were determined by fitting an analytical model to the PSF-subtracted images (McLure et al. 2000).

It is wise to pay attention to the fact that the values given in Table 3 of *Du03* do not fit the PA_{host} definition adopted here, contrary to what is claimed in the caption, but are determined with respect to the y-axis of the images. We have thus corrected these values applying a correction (the "ORIENTAT" parameter contained in the header of the observation files) taking account of the orientation of the HST with respect to the plane of the sky.

Fl04 (Floyd et al. 2004) Seventeen quasars with $z \in [0.29, 0.34]$ (both radio-loud and radio-quiet) were observed through the WF camera of the WFPC2 instrument on board the HST. The observations were carried in two photometric bands (the broad F814W and narrow F791W filters roughly corresponding to I band) in order to avoid the contamination by strong emission lines depending on the redshift of the object. The procedure used to derive the host galaxies parameters is the same as used in *Du03*.

It is clearly stated that the position angles of the studied hosts are given anticlockwise from the vertical in the images. We thus corrected these values in the same way as those of *Du03* and derived the corresponding PA_{host}.

Mc04 (McLure et al. 2004) 41 radio galaxies were observed in the I-band (F785LP filter) using the WF3 chip of the WFPC2. The redshift of the sample is comprised between $0.4 < z < 0.6$. The technique used to derive the host galaxies parameters is the same two-dimensional modeling process as the one used by *Du03*.

A.1.2. The near-IR domain

Ta96 (Taylor et al. 1996) Forty-four quasars were observed in the photometric K-band ($\lambda_{cent} \sim 2.2 \mu m$) using the IRCAM camera of the 3.9 m United Kingdom Infrared Telescope (UKIRT). The sample consists of RLQs, RQQs and RGs having a redshift around 0.2. Let us notice that the majority of these objetcs have been imaged in visible wavelengths by *Du03*. The parameters of the host galaxies were obtained using a fully two dimensional modeling procedure.

Pe01 (Percival et al. 2001) Thirteen objects spanning a redshift range of [0.26, 0.46] were observed in the K-band using the IRCAM3 camera of the UKIRT telescope. As the observations were carried out from the ground for relatively distant objects,

the host galaxies are completely hidden by the PSF wings of the nuclear component. Each image was then deconvolved to subtract a nuclear PSF and recover the weak glare of the underlying host-galaxy. The PSF-subtracted images were then modeled by a two-dimensional brightness analytical galaxy profile. The orientation of the host-galaxy (called α by *Pe01*) is given in their Table 4. It is expressed in radians and related to the PA$_{host}$ definition adopted in our paper following PA$_{host}$ = α (in degrees) +90 (or PA$_{host}$ = α −90 if α (in degrees) is smaller than 90°).

Gu06 (Guyon et al. 2006) Thirty-two quasars at $z < 0.3$ selected from the Palomar-Green Bright Quasar Survey were imaged in the near infrared domain (*H*-band) using adaptive optics (AO) imaging with the Gemini 8.2 m and Subaru 8.1 m telescopes on Mauna Kea. The images were PSF-subtracted and residuals were modeled using analytical galaxy models.

Ve06 (Veilleux et al. 2006) Thirty-three quasars were observed in the *H*-band using the Near Infrared Camera and Multi Object Spectrometer (NICMOS) instrument on board the HST. The sample consists of $z < 0.3$ luminous late-stage galactic mergers. The removal of the PSF and the structural parameters of the underlying hosts were determined using the GALFIT (Peng et al. 2002) algorithm.

A.2. Sample of new PA$_{host}$ data

A.2.1. The visible domain

Ba97 (Bahcall et al. 1997) The sample observed by *Ba97* contains 20 quasars $z < 0.3$ (both RQQs and RLQs) imaged with the WF3 camera of the WFPC2 instrument through the F606W filter (whose spectral characteristics are $\lambda_{cent} \sim 5900$ Å and $\Delta\lambda \sim 1500$ Å). Due to the redshift of the targets, powerful emission lines such as [OIII] and H$_\alpha$ are included in the image. The objects in the sample come from the 1991 Véron-Cetty & Véron catalog and were selected, such as $z \leq 0.2$, $M_V < -22.9$ et $|b| > 35°$ (where b stands for the galactic latitude). Several objects present in the sample were also part of the sample of *Du03* and were useful for assessing our PA$_{host}$ determination method (cf. Sect. 3.2.2).

Bo98 (Boyce et al. 1998) Seven quasars were imaged with the WFPC2 instrument on board the HST. Six of them were observed through the PC1 camera and the last one (PG0043+039) was observed using the WF chip. All the observations were taken through the F702W filter. The objects span a redshift range of $0.09 < z < 0.43$ and contain both RLQs and RQQs.

Ma03 (Marble et al. 2003) Twenty-nine RQQs spanning $0.136 < z < 0.596$ were observed with the PC1 camera of the WFPC2 instrument through the F814W. The targets were selected from the Two Micron All Sky Survey (2MASS) essentially according to color and galactic latitude criterion. Note that the 2MASS sample contains reddened type 1 quasars which, in the quasar unification scheme, can be interpreted as normal quasars, but seen close to the plane of an obscuring torus. The 2MASS objects have been classified as QSOs based on the fact that they are as luminous at 2.2 μm as QSOs in other samples (e.g. PG objects of comparable z).

Za06 (Zakamska et al. 2006) Nine type 2 radio-quiet quasars at $z \in [0.2, 0.4]$ were imaged through the Wide Field Channel (WFC) of the ACS instrument (Pavlovsky et al. 2005) in three photometric band (*Yellow*, *Blue* and *UV* cf. *Za06*). The resolution of the WFC is similar to the resolution of the PC1 camera of the WFPC2 instrument. Their targets were selected from the sample of type 2 AGN candidates unveiled by Zakamska et al. (2003) and Hao et al. (2005).

A.2.2. The near-IR domain

Ml01 (McLeod et al. 2001) Sixteen RLQs were imaged in the near-infrared domain (with the F160W filter corresponding approximately to H band), using the NIC2 camera (0.075″ pixel^{-1} resolution) of NICMOS on board the HST. The objects have $z < 0.4$ and were imaged in the MULTIACCUM mode (Schultz et al. 2005), which records data in a series of increasingly long nondestructive readouts, providing high dynamic unsaturated images.

Ku01 (Kukula et al. 2001) Twenty high-redshift ($z \in [0.83, 2.01]$) quasars were imaged using the NICMOS NIC1 camera (resolution of ~0.043″ pixel^{-1}). Due to the wide redshift range, two filters were used to image the quasars near the same rest-frame wavelength and to avoid the presence of strong emission lines, such as [OIII] and H$_\beta$. Thus the F110M filter (roughly *J*-band) was used to image the quasars in the $z \in [0.83, 1.00]$ range, and the F165M (roughly *H*-band) filter to image the quasars in the $z \in [1.67, 2.01]$ range.

Appendix B: Comparison with previous studies

In this Appendix we give some details on the comparison of the results obtained with the modeling procedure adopted in this paper and the results derived in published papers (listed in Sect. 2), since five objects of our *new* PA$_{host}$ *data* were previously studied. Hereafter, for each object of our sample that is also part of another study where host parameters were determined, we give a brief description of the object and compare the derived b/a and PA$_{host}$ obtained. In general we note good agreement between both sets of parameters.

PG 0052+251 The galaxy of this RQQ from the sample of *Ba97* consists in a spiral host with two prominent arms presenting several knots identified as HII regions. This object was already studied in two papers: Bahcall et al. (1996) (*Ba96*) and *Du03* (who noted that the galaxy profile was modeled best by a spheroidal component rather than a disk-like one). The results of these studies (PA = 173° et $b/a = 0.66$ for *Ba96* and PA = 175° et $b/a = 0.61$ for *Du03*) are very close to the one we obtain (PA = 171° and $b/a = 0.70$).

PHL 909 This RQQ host observed by *Ba97* was characterized in two previous studies: *Ba96* and McLure et al. 1999 (referred as *Du03* in our study). The host parameters of the elliptical galaxy we obtained with our method ($b/a = 0.51$ and PA = 129°) are similar to those found by both studies (*Ba96* found $b/a = 0.5$ and PA = 138° and *Du03* $b/a = 0.61$ and PA = 131°).

UM 357 This RQQ from the sample of NIR studied QSOs *Ml01* has been previously studied from the ground in a similar waveband by *Pe01*. The derived parameters using our technique (PA = 62° et b/a = 0.75) are close to those obtained by *Pe01* (PA = 56° and b/a = 0.66).

PG 1354+213 This RQQ was studied by *Pe01* in the K-band. In our sample, the observations of this object comes from the *Ml01* H-band survey. As the two images were taken in Near-IR, we can generally expect a good match between the K-band and H-band galaxy parameters. This is effectively the case for this object, for which *Pe01* gives PA = 169° and b/a = 0.89, while we obtain PA = 166° and b/a = 0.78.

PG 2233+134 The host-galaxy parameters were formerly derived by *Pe01* in the near-IR. They obtained PA = 178° and b/a = 0.8. These parameters are quite different from the one we obtained (PA = 135° and b/a = 0.89) using the *Ml01* images. However, as mentioned in the Table 2, our results do not satisfy the quality criterion defined in Sect. 3.2.2.